Mathematical and Computational Applications

MDPI

Article

Analytical Integration for Logarithmic Spatial Singularities in the Time Domain Boundary Element Method

Feng Zhao [1], Xiaokun Li [2], Juncheng Luo [1], Weidong Lei [3] and Hongjun Li [4,*]

[1] Guangzhou Metro Design & Research Institute Co., Ltd., Guangzhou 510410, China; zhaofeng3@dtsjy.com (F.Z.); luojuncheng@dtsjy.com (J.L.)
[2] China Nuclear Power Engineering Co., Ltd., Beijing 100840, China; lixka@cnpe.cc
[3] School of Intelligent Civil and Ocean Engineering, Harbin Institute of Technology Shenzhen, Shenzhen 518055, China; leiwd@hit.edu.cn
[4] Hebei Key Laboratory of Structural Safety and Low-Carbon Construction for Rural Buildings, Hebei Agricultural University, Baoding 071001, China
* Correspondence: chjlhj@hebau.edu.cn

Abstract

The treatment of logarithmic spatial singular integrals is a key challenge affecting the reliability of results when the time domain boundary element method (TD-BEM) is used to solve elastodynamic problems. To address this problem, this paper derives and establishes a set of analytically rigorous integration formulas for logarithmic spatial singularities based on the fundamental properties of the Heaviside function, which enables the direct spatiotemporal analytical solution of such singular integrals in TD-BEM. The formulas fill the research gap of the absence of direct analytical solutions for logarithmic spatial singular integrals in elastodynamic problems of TD-BEM, and enrich the theoretical system of the treatment of singular integrals for TD-BEM. Three typical elastodynamic engineering problems, including a fixed–fixed beam under a uniform sudden load, an infinite domain with a single cavity under a boundary blasting load, and a double tunnel beneath valley topography subjected to metro vibration load, are selected for numerical verification. The calculation results of the proposed method are compared with the reference solutions. It is shown that the calculation results of the proposed method are in good agreement with the reference solutions, which effectively verifies the correctness and engineering applicability of the analytical integration formulas.

Keywords: logarithmic spatial singularity; analytical integration; elastodynamics; time domain boundary element method

Check for updates

Academic Editor: Sascha Eisenträger

Received: 30 March 2026
Revised: 26 April 2026
Accepted: 28 April 2026
Published: 29 April 2026

Copyright: © 2026 by the authors. Licensee MDPI, Basel, Switzerland. This article is an open access article distributed under the terms and conditions of the Creative Commons Attribution (CC BY) license.

1. Introduction

With the growing demands of scientific computing and engineering simulation, the time domain boundary element method (TD-BEM) has exhibited unique advantages in solving wave propagation and transient dynamic problems as an efficient numerical analysis method. Compared with the finite element method (FEM) and the finite difference method (FDM), the boundary element method (BEM) features dimensionality reduction, which significantly reduces the computational degrees of freedom. In addition, the boundary integral equations of TD-BEM are constructed based on the full spatiotemporal fundamental solutions, endowing the method with an inherent ability to satisfy the radiation conditions at infinity. This makes TD-BEM naturally superior for solving problems involving infinite or semi-infinite boundaries. However, the treatment of singular integrals induced by the

singularities of fundamental solutions remains a critical challenge in the numerical implementation of TD-BEM. These singularities not only degrade the reliability of numerical solutions, but may also lead to unstable and even erroneous solutions [1,2], which restricts the further application and popularization of TD-BEM.

Within the framework of TD-BEM, singularities mainly originate from two sources. The first is the wavefront singularity, which manifests as abrupt changes in the displacement and stress fields near the wavefront due to the arrival of stress waves. The second is the strong or logarithmic spatial singularity, which arises from the infinite stress at the source point when a unit pulse is applied over an infinitesimal area. The presence of these two types of singularities is referred to as a dual singularity. Over the past decades, numerous scholars have proposed various methods to address singular integral problems in TD-BEM. For instance, Guiggiani et al. adopted local coordinate expansion to handle singular integrals [3,4], while Niu and Zhou applied regularization techniques to resolve strongly singular integrals in potential problems [5]. Xie et al. proposed the sinh transformation method for solving singular and nearly singular integral problems in the BEM analysis of thin-walled structures [6,7]. Giannopoulos and Anifantis [8] provides valuable insights into BEM-based modeling for interfacial phenomena and the treatment of singular behaviors. Mansur and Brebbia pioneered the use of Hadamard principal value integration to deal with wavefront singularities [9–14], which effectively improved the computational accuracy and efficiency and thus significantly promoted the development of TD-BEM. For spatial singularities, the rigid-body displacement method was once widely used by combining dynamic and static singularity characteristics. Nevertheless, this method is an indirect numerical approach that may lead to the accumulation of calculation errors. To achieve the direct resolution of spatial singularities in elastodynamics, Lei et al. [15,16], Xie et al. [17] and Zhong et al. [18] developed analytical integration methods that are independent of the rigid-body displacement method. However, these analytical methods are only applicable to strong singularities and not suitable for the integration of logarithmic spatial singularities. In the field of elastoplastic static analysis, the constant strain field method [19,20] and the initial stress expansion technique [21] are commonly used to treat spatial singularities. As noted by Telles et al. [19,20] and Banerjee et al. [21], these two methods require full-domain discretization, which impairs the inherent advantage of BEM in solving infinite-domain problems. Deng et al. [22] introduced the complementary theory into elastoplastic boundary integral equations, converting domain integrals into boundary integrals and transforming domain singularities to realize the solution of strongly singular domain integrals. This method retains the inherent advantages of BEM but is only applicable to elastoplastic static problems. For elastoplastic dynamic problems, Li et al. [23,24] applied analytical integration to directly handle singularities in TD-BEM and obtained stable and accurate calculation results, where only the boundaries and local plastic zones need to be discretized. Unfortunately, these analytical methods are still not applicable to logarithmic spatial singularities. In earlier years, Johnston and Elliott [25] proposed a generalized form of Telles' method [26], which optimizes the numerical solution of logarithmic singular integrals in BEM through arbitrary odd-order polynomial coordinate transformation, significantly improving computational accuracy and stability. Smith [27] developed direct Gauss quadrature formulas for isoparametric elements (linear, quadratic, and cubic elements), enabling efficient calculation of logarithmic singularities without separating singular terms. Both methods represent important contributions to the field. Nevertheless, these two methods essentially still rely on Gauss quadrature for numerical integration and do not establish a fully analytical solution path.

As the core cornerstone of the numerical implementation of TD-BEM, refining the theoretical system of singular integral treatment is crucial, as it represents a key prereq-

uisite for ensuring the reliability and accuracy of computational results. This paper first investigates the generation mechanism of logarithmic spatial singularities in TD-BEM and their influence on numerical solutions. On this basis, a direct analytical integration method for solving logarithmic spatial singular integrals is proposed by utilizing the fundamental properties of the Heaviside function. A set of formulas for logarithmic spatial singular integrals in TD-BEM are derived analytically. Unlike numerical strategies [26,27], the proposed method is completely free of numerical integration errors and is independent of mesh density and time-step refinement, thereby providing improved stability and reliability in dynamic analysis. Three typical numerical examples covering finite, infinite, and semi-infinite domains are designed to verify the correctness and applicability of the proposed formulas. The robustness of the TD-BEM, incorporating the proposed formulas, has also been verified through an infinite-domain example.

2. Displacement Boundary Integral Equation

The formulas proposed in the paper are applicable for the plane strain problems without body force in elastodynamics. Once the elastic modulus E and Poisson's ratio ν are replaced by $(1+2\nu)E/(1+\nu)^2$ and $\nu/(1+\nu)$, the formulas for plane stress problems can be obtained. The displacement boundary integral equation in the Cartesian coordinate system $O-x_1x_2$ is shown in Equation (1), which is also presented in [11].

$$c_{ik}u_i(P,t) = -\int_\Gamma \int_0^t p^*_{ik}(P,\tau;Q,t)u_k(Q,\tau)\mathrm{d}\tau\mathrm{d}\Gamma(Q) + \int_\Gamma \int_0^t u^*_{ik}(P,\tau;Q,t)p_k(Q,\tau)\mathrm{d}\tau\mathrm{d}\Gamma(Q) \tag{1}$$

where P and τ represent the source point and excitation instant of the unit impulse, respectively; Q and t represent the field point and the observation instant, respectively; c_{ik} represents position coefficient of the source point P, as given in Equation (2); u^*_{ik} and p^*_{ik} represent the displacement and surface traction fundamental solutions, respectively, as presented in Equations (3) and (4).

$$c_{ik} = \begin{cases} \delta_{ik} & P \in \Omega \text{ (Inner points)} \\ \frac{1}{2}\delta_{ik} & P \in \Gamma \text{ (Smooth boundary points)} \\ \delta_{ik} + \lim\limits_{\varepsilon\to 0}\int_{\Gamma_\varepsilon} p^*_{\mathrm{s},ik}\mathrm{d}\Gamma & P \in \Gamma \text{ (Non smooth boundary points)} \end{cases} \tag{2}$$

where δ_{ik} is Kronecker delta; $p^*_{\mathrm{s},ik}$ represents the surface traction for elastostatics [20]; Γ_ε is a circular arc centered at point P with radius ε, as shown in Figure 1; θ_1 and θ_2 are the angles between the positive direction of the x_1-axis and the outer normal of the tangents on both sides of point P, respectively, with positive values for counterclockwise directions and negative values for clockwise directions.

$$u^*_{ik}(P,\tau;Q,t) = \frac{1}{2\pi\rho v_\mathrm{s}}[(E_{ik}L_\mathrm{s} + F_{ik}L_\mathrm{s}^{-1} + J_{ik}L_\mathrm{s}N_\mathrm{s})H_\mathrm{s} - \frac{v_\mathrm{s}}{v_\mathrm{d}}(F_{ik}L_\mathrm{d}^{-1} + J_{ik}L_\mathrm{d}N_\mathrm{d})H_\mathrm{d}] \tag{3}$$

$$\begin{aligned} p^*_{ik}(P,\tau;Q,t) = \; & \tfrac{1}{2\pi\rho v_s}\{A_{ik}(rL_s^3H_s - L_s\delta_s) + B_{ik}L_sN_sH_s + D_{ik}(rL_s^3H_s - \tfrac{L_sN_s}{r^2}\delta_s) \\ & - \tfrac{v_s}{v_d}[B_{ik}L_dN_dH_d + D_{ik}(rL_d^3H_d - \tfrac{L_dN_d}{r^2}\delta_d)]\} \end{aligned} \tag{4}$$

where v_d and v_s denote the velocities of the P-wave (primary wave) and S-wave (shear wave), respectively; r represents the distance between source point P and the field point Q; the other parameters in Equations (3) and (4) are as follows:

$$
\begin{aligned}
A_{ik} &= \mu(2\varphi r_{,i}\, n_k + \delta_{ik}\tfrac{\partial r}{\partial n} + r_{,k}\, n_i) \\
B_{ik} &= -\tfrac{2\mu}{r^3}(\delta_{ik}\tfrac{\partial r}{\partial n} + r_{,i}\, n_k + r_{,k}\, n_i - 4\tfrac{\partial r}{\partial n} r_{,i}\, r_{,k}) \\
D_{ik} &= -2\mu(\varphi r_{,i}\, n_k + \tfrac{\partial r}{\partial n} r_{,i}\, r_{,k}) \\
E_{ik} &= \delta_{ik} \\
F_{ik} &= \tfrac{\delta_{ik}}{r^2} \\
J_{ik} &= -\tfrac{r_{,i} r_{,k}}{r^2} \\
r_{,l} &= \tfrac{\partial r}{\partial x_l^Q} = -\tfrac{\partial r}{\partial x_l^P} \\
n_l &= \cos(x_l, n) \\
\tfrac{\partial r}{\partial n} &= r_{,l} n_l \\
H_w &= H[v_w(t-\tau) - r] \\
\delta_w &= \delta[v_w(t-\tau) - r] \\
L_w &= [v_w^2(t-\tau)^2 - r^2]^{-\frac{1}{2}} \\
N_w &= 2v_w^2(t-\tau)^2 - r^2
\end{aligned}
$$

where μ and λ are Lamé constants, and $\varphi = \lambda/2\mu$; n is the outward unit normal of the boundary of interior domain; subscripts $i, k, l = 1, 2$ correspond to the x_1 and x_2 directions, respectively; w takes "d" and "s" to denote P-wave and S-wave, respectively.

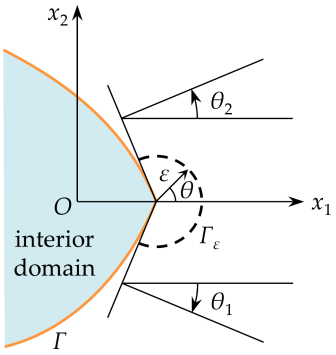


Figure 1. The case where P is located at boundary.

3. Numerical Implementations

The boundary element integral equation for elastodynamics needs to be discretized in both time and space. The mesh length and time step are determined with reference to the research findings of Mansur and Brebbia [10].

3.1. Time-Discretization

The time domain $[0, t]$ is divided into M intervals with a time step of $\Delta t = t/M$. The time nodes are defined as $t_m = m\Delta t$, where $m = 0, 1, 2, \ldots, M$. Within each interval, the surface traction is assumed to be constant, while the displacement varies linearly. This assumption is suitable for loads with time jumps [28,29], and is applicable for loads without time jumps when the time step is small [15]. The surface traction $p_k^{(m)}(Q, \tau)$ and displacement $u_k^{(m)}(Q, \tau)$ of the field point Q at time τ within the interval $[t_{m-1}, t_m]$ can be expressed represented by the time node variables p_k^m and $u_k^{(m,a)}$ using an interpolation method, as given in Equation (5).

$$
\begin{cases}
p_k^{(m)}(Q, \tau) = p_k^m \\
u_k^{(m)}(Q, \tau) = \sum_{a=1}^{2} \Psi_a^m u_k^{(m,a)}
\end{cases}
\tag{5}
$$

with

$$\begin{cases} \Psi_1^m(\tau) = \frac{t_m - \tau}{\Delta t} \\ \Psi_2^m(\tau) = \frac{\tau - t_{m-1}}{\Delta t} \end{cases} \tag{6}$$

3.2. Space-Discretization

Assuming that the boundary is discretized into n_e linear boundary elements, for the field point Q within the boundary element e, the surface traction $p_k^{(m;e)}(Q,\tau)$ and displacement $u_k^{(m;e)}(Q,\tau)$ vary within the element. They can be represented by the element node variables $p_k^{(m;e,b)}$ and $u_k^{(m,a;e,b)}$;

$$\begin{cases} p_k^{(m;e)}(Q,\tau) = \sum\limits_{b=1}^{2} p_k^{(m;e,b)} N_b(\xi) \\ u_k^{(m;e)}(Q,\tau) = \sum\limits_{b=1}^{2} \sum\limits_{a=1}^{2} \Psi_a^m u_k^{(m,a;e,b)} N_b(\xi) \end{cases} \tag{7}$$

where $N_1(\xi)$ and $N_2(\xi)$ are the shape functions, as given in Equation (8).

$$\begin{cases} N_1(\xi) = \frac{1}{2}(1-\xi) \\ N_2(\xi) = \frac{1}{2}(1+\xi) \end{cases} \tag{8}$$

3.3. The Discretization of Boundary Element Integral Equation

The discrete expressions of integrals in Equation (1) are detailed in Equation (9).

$$\begin{cases} \int_\Gamma \int_0^t u_{ik}^* p_k \mathrm{d}\tau \mathrm{d}\Gamma = \sum\limits_{e=1}^{n_e} \sum\limits_{m=1}^{M} \sum\limits_{b=1}^{2} g_{ik}^{(m;e,b)} p_k^{(m;e,b)} \\ \int_\Gamma \int_0^t p_{ik}^* u_k \mathrm{d}\tau \mathrm{d}\Gamma = \sum\limits_{e=1}^{n_e} \sum\limits_{m=1}^{M} \sum\limits_{b=1}^{2} \sum\limits_{a=1}^{2} \overline{h}_{ik}^{(m,a;e,b)} u_k^{(m,a;e,b)} \end{cases} \tag{9}$$

where $g_{ik}^{(m;e,b)}$ and $\overline{h}_{ik}^{(m,a;e,b)}$ denote the influence coefficients of surface traction and displacement of the field point Q at instant t_m on the displacement of source point P at instant t, as given in Equation (10).

$$\begin{cases} g_{ik}^{(m;e,b)} = \int_{\Gamma_e} \int_{t_{m-1}}^{t_m} u_{ik}^* N_b \mathrm{d}\tau \mathrm{d}\Gamma \\ \overline{h}_{ik}^{(m,a;e,b)} = \int_{\Gamma_e} \int_{t_{m-1}}^{t_m} p_{ik}^* \Psi_a^m N_b \mathrm{d}\tau \mathrm{d}\Gamma \end{cases} \tag{10}$$

4. Solution of Element Influence Coefficients

The influence coefficient $\overline{h}_{ik}^{(m,a;e,b)}$ has been calculated in reference [16]; therefore, only $g_{ik}^{(m;e,b)}$ is solved in this study.

Singularities in $g_{ik}^{(m;e,b)}$ arise from two primary sources. The first is the *wavefront singularity*, which has the mathematical form $[v_w(t-\tau) - r]^{-n/2} \to \infty$. This type of singularity corresponds to abrupt variations in the response near the wavefront, caused by the arrival of stress waves. The second is the *logarithmic spatial singularity*, expressed as $\ln r \to \infty$, which results from a unit pulse applied over an infinitesimal area. Both wavefront and logarithmic spatial singularities occur in elements where the node coincides with the source point P, whereas only the wavefront singularity appears in other elements.

According to the singularity types contained in the integrals of the influence coefficients, different integration schemes are employed. For integrals involving only wavefront singularities, the Hadamard principal value integration is adopted for temporal integration and Gauss quadrature for spatial integration. For integrals containing logarithmic spatial

singularities, the direct analytical integration method is used for both temporal and spatial integration. For nonsingular integrals, Riemann integration is applied for temporal integration, while Gauss quadrature is used for spatial integration.

4.1. Influence Coefficients Without Spatial Singularity

When the source point P does not coincide with the field point Q, we have $r \neq 0$, as illustrated in Figure 2. In this case, no logarithmic spatial singularity exists; that is, $\ln r$ remains finite. Only the wavefront singularity occurs, expressed as $[v_w(t-\tau)-r]^{-n/2} \to \infty$.

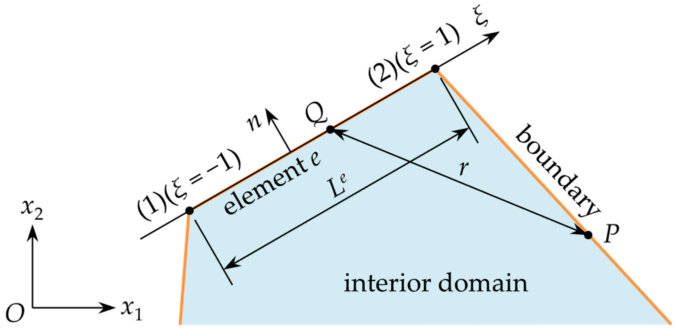


Figure 2. The source point P does not coincide with the field point Q of element e.

4.1.1. The Expression of Kernel Functions

The form of $g_{ik}^{(m;e,b)}$ can be obtained by substituting Equation (3) into Equation (10), as given in Equation (11).

$$g_{ik}^{(m;e,b)} = \frac{1}{2\pi\rho v_s^2}\int_{\Gamma_e}[(E_{ik}a_s^m + F_{ik}b_s^m + J_{ik}c_s^m) - \frac{v_s^2}{v_d^2}(F_{ik}b_d^m + J_{ik}c_d^m)]N_b \mathrm{d}\Gamma \tag{11}$$

where a_w^m, b_w^m and c_w^m are the kernel functions related to time and space, as follows:

$$\begin{aligned} a_w^m &= \int_{t_{m-1}}^{t_m} v_w L_w H_w \mathrm{d}\tau \\ b_w^m &= \int_{t_{m-1}}^{t_m} v_w L_w^{-1} H_w \mathrm{d}\tau \\ c_w^m &= \int_{t_{m-1}}^{t_m} v_w L_w N_w H_w \mathrm{d}\tau \end{aligned}$$

4.1.2. Temporal Integration for Kernel Functions

The coefficients A_{w1}~A_{w6} are introduced to simplify the expression, which are dependent on $M-m$.

$$\begin{aligned} A_{w1} &= \sqrt{v_w(t-t_{m-1})-r} & A_{w2} &= \sqrt{v_w(t-t_{m-1})+r} & A_{w5} &= v_w(t-t_{m-1}) \\ A_{w3} &= \sqrt{v_w(t-t_m)-r} & A_{w4} &= \sqrt{v_w(t-t_m)+r} & A_{w6} &= v_w(t-t_m) \end{aligned}$$

According to the properties of Heaviside function, the relationship between the singular time t_{rw} as $t_{rw} = t - r/v_w$ and time interval $[t_{m-1}, t_m]$ can be classified into the following four types. The kernel functions can be calculated correspondingly.

1. For $t_m \leq t_{rw}$ and $\tau \in [t_{m-1}, t_m]$, one has $M_w \geq 0$ and $H_w = 1$

$$\begin{aligned} a_w^m &= \ln|L_w^{-1} - v_w(t-\tau)|_{t_{m-1}}^{t_m} = \ln\tfrac{A_{w1}A_{w2}+A_{w5}}{A_{w3}A_{w4}+A_{w6}} \\ b_w^m &= -\tfrac{1}{2}[r^2\ln|L_w^{-1} - v_w(t-\tau)| + v_w(t-\tau)L_w^{-1}]|_{t_{m-1}}^{t_m} \\ &= -\tfrac{1}{2}[r^2 a_w^m + (A_{w3}A_{w4}A_{w6} - A_{w1}A_{w2}A_{w5})] \\ c_w^m &= -v_w(t-\tau)L_w^{-1}|_{t_{m-1}}^{t_m} = -A_{w3}A_{w4}A_{w6} + A_{w1}A_{w2}A_{w5} \end{aligned}$$

2. For $t_{m-1} < t_{rw} < t_m$ and $\tau \in [t_{m-1}, t_{rw}]$, one has $M_w \geq 0$ and $H_w = 1$; for $t_{m-1} < t_{rw} < t_m$ and $\tau \in (t_{rw}, t_m]$, one has $M_w < 0$ and $H_w = 0$

$$a_w^m = \ln|L_w^{-1} - v_w(t-\tau)|_{t_{m-1}}^{t_{rw}} = \ln\frac{A_{w1}A_{w2} + A_{w5}}{r}$$
$$b_w^m = -\frac{1}{2}[r^2 \ln|L_w^{-1} - v_w(t-\tau)| + v_w(t-\tau)L_w^{-1}]|_{t_{m-1}}^{t_{rw}} = -\frac{1}{2}(r^2 a_w^m - A_{w1}A_{w2}A_{w5})$$
$$c_w^m = -v_w(t-\tau)L_w^{-1}|_{t_{m-1}}^{t_{rw}} = A_{w1}A_{w2}A_{w5}$$

3. For $t_{m-1} \geq t_{rw}$ and $\tau \in [t_{m-1}, t_m]$, one has $M_w < 0$ and $H_w = 0$

$$a_w^m = b_w^m = c_w^m = 0$$

4.1.3. Spatial Integration for Influence Coefficients

After substituting the kernel functions into Equation (11), the Gauss quadrature is employed to perform the spatial integration of the influence coefficients. The calculation formula is given as Equation (12).

$$\int_{\Gamma_e} f(r)N_b \mathrm{d}\Gamma = \sum_{g=1}^{ng} \frac{L^e}{2} f[r(\xi_g)]N_b(\xi_g)\omega_g \tag{12}$$

where ξ_g and ω_g are Gauss quadrature point and weight, representatively; ng is the number of Gaussian integration points; $r(\xi_g)$ represents the distance between the field point Q and the source point P corresponding to ξ_g, as shown in Equation (13).

$$\begin{cases} r(\xi_g) = \sqrt{[x_1(\xi_g) - x_1^P]^2 + [x_2(\xi_g) - x_2^P]^2} \\ x_m(\xi_g) = \sum_{b=1}^{2} N_b(\xi_g)x_m^{(b)}, \ m = 1, 2 \end{cases} \tag{13}$$

4.2. Influence Coefficients with Logarithmic Spatial Singularity

When point P coincides with a node of element e, the distance r varies from 0 to L^e. Figure 3 illustrates the case where P coincides with the first node of the element. As $r \to 0$, logarithmic spatial singularity occurs, i.e., $\ln r \to \infty$.

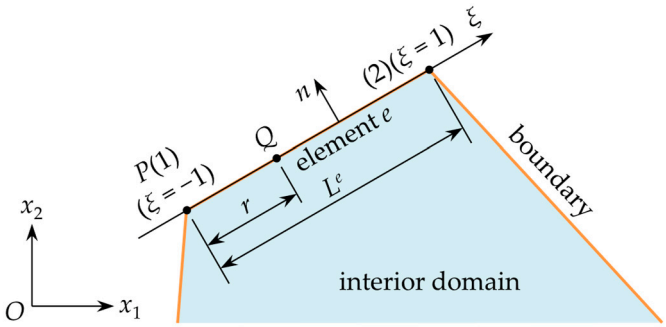


Figure 3. The source point P is coincident with the first node of element e.

4.2.1. Separation of Singular Integral Part

Under the condition shown in Figure 3, the expression of local coordinated ξ can be derived as Equation (14).

$$\xi = \frac{2r}{L^e} - 1 \tag{14}$$

Substituting Equation (14) into shape function Equation (8), yields:

$$\begin{cases} N_1 = 1 - \frac{r}{L^e} \\ N_2 = \frac{r}{L^e} \end{cases} \tag{15}$$

The differential $\mathrm{d}\Gamma$ transforms into

$$\mathrm{d}\Gamma = \mathrm{d}r \tag{16}$$

Substituting Equations (15) and (16) into Equation (11), the influence coefficient $g_{ik}^{(m;e,b)}$ becomes:

$$g_{ik}^{(m;e,1)} = \frac{1}{2\pi\rho v_s^2}\int_0^{L^e}[(E_{ik}a_s^m + F_{ik}b_s^m + J_{ik}c_s^m) - \frac{v_s^2}{v_d^2}(F_{ik}b_d^m + J_{ik}c_d^m)](1 - \frac{r}{L^e})\mathrm{d}r \tag{17}$$

$$g_{ik}^{(m;e,2)} = \frac{1}{2\pi\rho v_s^2}\int_0^{L^e}[(E_{ik}a_s^m + F_{ik}b_s^m + J_{ik}c_s^m) - \frac{v_s^2}{v_d^2}(F_{ik}b_d^m + J_{ik}c_d^m)]\frac{r}{L^e}\mathrm{d}r \tag{18}$$

There is no spatial singularity in $g_{ik}^{(m;e,2)}$, whereas logarithmic spatial singularity exists in $g_{ik}^{(m;e,1)}$. The method presented in Section 4.1 can be adopted to address $g_{ik}^{(m;e,2)}$, while $g_{ik}^{(m;e,1)}$ needs to be decomposed into a nonsingular part $g_{ik}^{\mathrm{n}(m;e,1)}$ and a logarithmic singular part $g_{ik}^{\mathrm{s}(m;e,1)}$. Singular integrals are decomposed into singular and non-singular components due to their distinct solution characteristics. The nonsingular component can be directly calculated by conventional numerical integration methods such as Gaussian quadrature, while the singular component cannot be evaluated by ordinary numerical quadrature and thus requires dedicated treatment. In this work, an analytical solution method is proposed for the singular component. The $g_{ik}^{\mathrm{n}(m;e,1)}$ is the opposite of $g_{ik}^{(m;e,2)}$, and the expression for $g_{ik}^{\mathrm{s}(m;e,1)}$ is given

$$g_{ik}^{\mathrm{s}(m;e,1)} = \frac{1}{2\pi\rho v_s^2}\int_0^{L^e}[(E_{ik}a_s^m + F_{ik}b_s^m + J_{ik}c_s^m) - \frac{v_s^2}{v_d^2}(F_{ik}b_d^m + J_{ik}c_d^m)]\mathrm{d}r \tag{19}$$

Similar results can be obtained when the source point P coincides with the 2nd node of element e. Once the singular part $g_{ik}^{\mathrm{s}(m;e,1)}$ is solved, all the influence coefficients can be obtained.

4.2.2. The Calculation of the Singular Integral Part

1. The time-space integral domain and kernel functions

The area filled with dots in Figure 4 is the time-space integral domain of the kernel functions, and its mathematical form is given by Equation (20).

$$D_{\tau r} = \{(\tau, r)|\tau \in [t_{m-1}, t_m],\ r \in [0, \min(v_w(t-\tau), L^e)]\} \tag{20}$$

In Figure 4, $r_1 = c_w(t - t_{m-1})$, $r_2 = c_w(t - t_m)$ and $t_{Lw} = t - \frac{L^e}{c_w}$ are defined; the integral domain $D_{\tau r}$ can be classified into the following three types:

- Rectangular domain ①: $D_{\tau r} = \{(\tau, r)|\tau \in [t_{m-1}, t_m],\ r \in [0, L^e]\}$;
- Trapezoidal domain ②: $D_{\tau r} = \{(\tau, r)|\tau \in [t_{m-1}, t_m],\ r \in [0, v_w(t-\tau)]\}$;
- Mixed domain ③: $D_{\tau r} = \{(\tau, r)|\tau \in [t_{m-1}, t_{Lw}],\ r \in [0, L^e];\ \tau \in [t_{Lw}, t_m],\ r \in [0, v_w(t-\tau)]\}$.

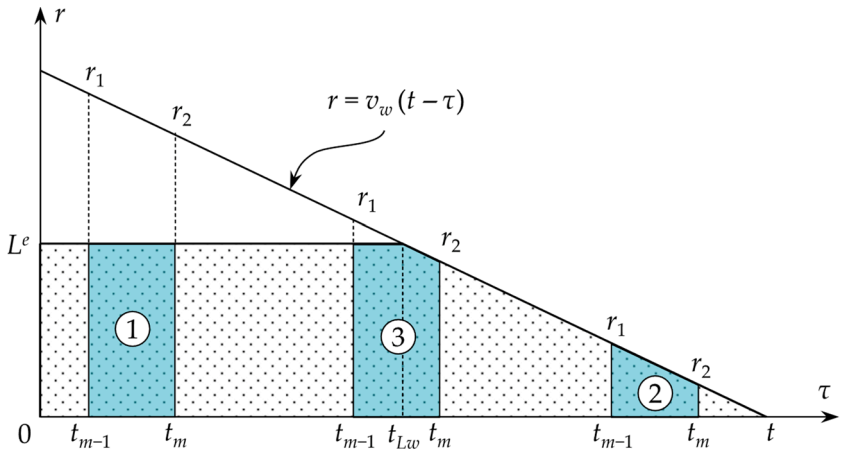


Figure 4. Three types of spatiotemporal integral domain.

All three types of integral domains are suitable for the integration order of integrating with respect to r first and then τ. By interchanging the order of integration in Equation (19), we get

$$\begin{aligned} g_{ik}^{\mathrm{s}(m;e,1)} &= \frac{1}{2\pi\rho v_{\mathrm{s}}^2}\int_{t_{m-1}}^{t_m}[E_{ik}^0 a_{\mathrm{s}} + F_{ik}^0 b_{\mathrm{s}} + J_{ik}^0 c_{\mathrm{s}} - \frac{v_{\mathrm{s}}^2}{v_{\mathrm{d}}^2}(F_{ik}^0 b_{\mathrm{d}} + J_{ik}^0 c_{\mathrm{d}})]\mathrm{d}\tau \\ &= \frac{1}{2\pi\rho v_{\mathrm{s}}^2}\int_{t_{m-1}}^{t_m}[E_{ik}^0 a_{\mathrm{s}} + F_{ik}^0 (b_{\mathrm{s}} - \frac{v_{\mathrm{s}}^2}{v_{\mathrm{d}}^2} b_{\mathrm{d}}) + J_{ik}^0 (c_{\mathrm{s}} - \frac{v_{\mathrm{s}}^2}{v_{\mathrm{d}}^2} c_{\mathrm{d}})]\mathrm{d}\tau \\ &= \frac{1}{2\pi\rho v_{\mathrm{s}}^2}[E_{ik}^0 I a_{\mathrm{s}} + F_{ik}^0 (I b_{\mathrm{s}} - \frac{v_{\mathrm{s}}^2}{v_{\mathrm{d}}^2} I b_{\mathrm{d}}) + J_{ik}^0 (I c_{\mathrm{s}} - \frac{v_{\mathrm{s}}^2}{v_{\mathrm{d}}^2} I c_{\mathrm{d}})] \end{aligned} \tag{21}$$

with

$$\begin{aligned} E_{ik}^0 &= F_{ik}^0 = \delta_{ik} \\ J_{ik}^0 &= -r_{,i} r_{,k} \\ a_w &= \int_{\Gamma_e} v_w L_w H_w \mathrm{d}\Gamma \\ b_w &= \int_{\Gamma_e} v_w \frac{L_w^{-1}}{r^2} H_w \mathrm{d}\Gamma \\ c_w &= \int_{\Gamma_e} v_w \frac{L_w N_w}{r^2} H_w \mathrm{d}\Gamma \\ I a_w &= \int_{t_{m-1}}^{t_m} a_w \mathrm{d}\tau \\ I b_w &= \int_{t_{m-1}}^{t_m} b_w \mathrm{d}\tau \\ I c_w &= \int_{t_{m-1}}^{t_m} c_w \mathrm{d}\tau \end{aligned}$$

The solution method for each integral domain is described as follows. For the rectangular and trapezoidal domain, the integral bounds of τ are firstly determined as t_{m-1} to t_m. Within each time interval of τ, the lower limit of r is fixed at 0, and the upper limit is defined as L^e for rectangular domain and $v_w(t-\tau)$ for trapezoidal domain. After completing the integration over r, the integral with respect to τ is performed sequentially. For the mixed integral domain, the entire region is first divided into independent rectangular and trapezoidal subdomains with t_{Lw} as the boundary. Each subdomain is calculated separately following the corresponding integration rules for rectangular and trapezoidal domains.

In terms of singularity characteristics, only logarithmic spatial singularity exists in rectangular domains. In contrast, both trapezoidal and mixed domains contain logarithmic spatial singularity and wavefront singularity simultaneously, leading to stronger singular behavior. Such higher-order singularities have a more significant influence on the stability

and accuracy of the numerical results. Therefore, appropriate treatment of trapezoidal and mixed integral domains is essential to ensure the reliability of the TD-BEM solution.

2. Spatial integration of kernel functions

The spatial integrations of the kernel functions are evaluated by analytical integration method according to the type of integral domain.

- For the case $r_2 \geq L^e$, $D_{\tau r}$ becomes a rectangular domain ①, with $r \in [0, L^e]$

$$a_w = v_w \arctan \frac{L^e}{\sqrt{v_w^2(t-\tau)^2-(L^e)^2}}$$
$$b_w = -v_w[\frac{L_w^{-1}}{r} + \arctan(rL_w)]|_{r=0}^{r=L^e} = b_w^{\text{up}} - b_w^{\text{low}}$$
$$c_w = 2b_w + a_w$$

where b_w^{up} and b_w^{low} denote the upper and lower integral limits of b_w, with their expressions given below.

$$b_w^{\text{up}} = -v_w \frac{L_w^{-1}}{r}|_{r=L^e} - a_w$$
$$b_w^{\text{low}} = -v_w \frac{L_w^{-1}}{r}|_{r=0}$$

Since

$$b_{\text{s}}^{\text{low}} - \frac{v_{\text{s}}^2}{v_{\text{d}}^2} b_{\text{d}}^{\text{low}} = -\lim_{r\to 0} \frac{v_{\text{s}}^2 v_s}{r}(\frac{L_{\text{s}}^{-1}}{v_{\text{s}}} - \frac{L_{\text{d}}^{-1}}{v_{\text{d}}}) = \lim_{r\to 0} \frac{1}{2(t-\tau)}(1 - \frac{v_{\text{s}}^2}{v_{\text{d}}^2})r = 0$$

only the upper integral limit of b_w needs to be considered. Further derivation leads to:

$$a_{\text{s}} - \frac{v_{\text{s}}^2}{v_{\text{d}}^2} a_{\text{d}} = v_{\text{s}}^2(\frac{1}{v_{\text{s}}} \arctan \frac{L^e}{\sqrt{v_{\text{s}}^2(t-\tau)^2-(L^e)^2}} - \frac{1}{v_{\text{d}}} \arctan \frac{L^e}{\sqrt{v_{\text{d}}^2(t-\tau)^2-(L^e)^2}})$$
$$b_{\text{s}} - \frac{v_{\text{s}}^2}{v_{\text{d}}^2} b_{\text{d}} = b_{\text{s}}^{\text{up}} - \frac{v_{\text{s}}^2}{v_{\text{d}}^2} b_{\text{d}}^{\text{up}} = -\frac{v_{\text{s}}^2}{r}(\frac{L_{\text{s}}^{-1}}{v_{\text{s}}} - \frac{L_{\text{d}}^{-1}}{v_{\text{d}}})|_{r=L^e} - (a_{\text{s}} - \frac{v_{\text{s}}^2}{v_{\text{d}}^2} a_{\text{d}})$$
$$c_{\text{s}} - \frac{v_{\text{s}}^2}{v_{\text{d}}^2} c_{\text{d}} = 2(b_{\text{s}} - \frac{v_{\text{s}}^2}{v_{\text{d}}^2} b_{\text{d}}) + (a_{\text{s}} - \frac{v_{\text{s}}^2}{v_{\text{d}}^2} a_{\text{d}}) = -2\frac{v_{\text{s}}^2}{r}(\frac{L_{\text{s}}^{-1}}{v_{\text{s}}} - \frac{L_{\text{d}}^{-1}}{v_{\text{d}}})|_{r=L^e} - (a_{\text{s}} - \frac{v_{\text{s}}^2}{v_{\text{d}}^2} a_{\text{d}})$$

- For the case $r_1 \leq L^e$, $D_{\tau r}$ becomes a trapezoidal domain ②, with $r \in [0, v_w(t-\tau)]$

$$a_w = \frac{\pi}{2} v_w$$
$$a_{\text{s}} - \frac{v_{\text{s}}^2}{v_{\text{d}}^2} a_{\text{d}} = \frac{\pi}{2} v_{\text{s}} - \frac{v_{\text{s}}^2}{v_{\text{d}}^2} \frac{\pi}{2} v_{\text{d}} = \frac{\pi}{2} v_{\text{s}}^2(\frac{1}{v_{\text{s}}} - \frac{1}{v_{\text{d}}})$$
$$b_{\text{s}} - \frac{v_{\text{s}}^2}{v_{\text{d}}^2} b_{\text{d}} = c_{\text{s}} - \frac{v_{\text{s}}^2}{v_{\text{d}}^2} c_{\text{d}} = -\frac{\pi}{2} v_{\text{s}}^2(\frac{1}{v_{\text{s}}} - \frac{1}{v_{\text{d}}})$$

- For the case $r_2 < L^e$ and $r_1 > L^e$, $D_{\tau r}$ becomes a mixed domain ③,

The integral over $\tau \in [t_{m-1}, t_{Lw})$ can be evaluated by the method for the rectangular domain, and the over $\tau \in [t_{Lw}, t_m]$ by the method for the trapezoidal domain.

3. Temporal integration of kernel functions

After obtaining the spatial integration results, the temporal integration of kernel functions over $\tau \in [t_{m-1}, t_m]$ can be performed. Coefficients B_{w1}~B_{w6} are introduced to simplify the expressions, which depend on $M - m$, as follows.

$$B_{w1} = \sqrt{v_w(t-t_{m-1}) - L^e} \quad B_{w2} = \sqrt{v_w(t-t_m) + L^e} \quad B_{w5} = v_w(t-t_{m-1})$$
$$B_{w3} = \sqrt{v_w(t-t_m) - L^e} \quad B_{w4} = \sqrt{v_w(t-t_m) + L^e} \quad B_{w6} = v_w(t-t_m)$$

- Rectangular domain ①, with $r \in [0, L^e]$

$$Ia_w = \int_{t_{m-1}}^{t_m} a_w \mathrm{d}\tau = -B_{w6} \arctan\frac{L^e}{B_{w3}B_{w4}} + L^e \ln\frac{B_{w6} - B_{w3}B_{w4}}{B_{w5} - B_{w1}B_{w2}} + B_{w5} \arctan\frac{L^e}{B_{w1}B_{w2}}$$

$$\begin{aligned} Ib_\mathrm{s} - \frac{v_\mathrm{s}^2}{v_\mathrm{d}^2} Ib_\mathrm{d} &= \int_{t_{m-1}}^{t_m} (b_\mathrm{s} - \frac{v_\mathrm{s}^2}{v_\mathrm{d}^2} b_\mathrm{d}) \mathrm{d}\tau \\ &= \frac{1}{2}\left(\frac{B_{\mathrm{s}3}B_{\mathrm{s}4}B_{\mathrm{s}6} - B_{\mathrm{s}1}B_{\mathrm{s}2}B_{\mathrm{s}5}}{L^e} + L^e \ln\frac{B_{\mathrm{s}6} - B_{\mathrm{s}3}B_{\mathrm{s}4}}{B_{\mathrm{s}5} - B_{\mathrm{s}1}B_{\mathrm{s}2}}\right) \\ &\quad -\frac{1}{2}\frac{v_\mathrm{s}^2}{v_\mathrm{d}^2}\left(\frac{B_{\mathrm{d}3}B_{\mathrm{d}4}B_{\mathrm{d}6} - B_{\mathrm{d}1}B_{\mathrm{d}2}B_{\mathrm{d}5}}{L^e} + L^e \ln\frac{B_{\mathrm{d}6} - B_{\mathrm{d}3}B_{\mathrm{d}4}}{B_{\mathrm{d}5} - B_{\mathrm{d}1}B_{\mathrm{d}2}}\right) \\ &\quad -(Ia_\mathrm{s} - \frac{v_\mathrm{s}^2}{v_\mathrm{d}^2} Ia_\mathrm{d}) \end{aligned}$$

$$Ic_\mathrm{s} - \frac{v_\mathrm{s}^2}{v_\mathrm{d}^2} Ic_\mathrm{d} = 2(Ib_\mathrm{s} - \frac{v_\mathrm{s}^2}{v_\mathrm{d}^2} Ib_\mathrm{d}) + (Ia_\mathrm{s} - \frac{v_\mathrm{s}^2}{v_\mathrm{d}^2} Ia_\mathrm{d})$$

- Trapezoidal domain ②, with $r_1 \leq L^e$

$$\begin{aligned} Ia_w &= \tfrac{\pi}{2} v_w \Delta t \\ Ib_\mathrm{s} - \tfrac{v_\mathrm{s}^2}{v_\mathrm{d}^2} Ib_\mathrm{d} &= Ic_\mathrm{s} - \tfrac{v_\mathrm{s}^2}{v_\mathrm{d}^2} Ic_\mathrm{d} = -(Ia_\mathrm{s} - \tfrac{v_\mathrm{s}^2}{v_\mathrm{d}^2} Ia_\mathrm{d}) \end{aligned}$$

- Mixed domain ③, with $r_2 < L^e$ and $r_1 > L^e$

For $\tau \in [t_1, t_{Lw})$, the temporal integration can be performed simply by replacing the upper limit t_2 with t_{Lw} in the formulas of Case ①; for $\tau \in [t_{Lw}, t_2]$, it can be done by replacing the lower limit t_1 with t_{Lw} in the formulas of Case ②. The kernel functions can be obtained by summing the two solutions.

$g_{ik}^{\mathrm{s}(m;e,1)}$ can be evaluated by substituting the kernel functions and coefficients E_{ik}^0, F_{ik}^0 and J_{ik}^0 into Equation (21).

5. Assembly and Solution

5.1. Assembly

By sequentially aligning the source point P with each boundary node, the element influence coefficients for all elements can be determined. After assembling the element influence coefficients in both time and space, the algebraic equation system corresponding to the boundary integral equation is formed. The matrix form of algebraic equation system is given in Equation (22).

$$\mathbf{H}^{MM}\mathbf{u}^M = \mathbf{G}^{MM}\mathbf{p}^M + \mathbf{a}^M \tag{22}$$

where $\mathbf{H}^{MM}$ is the displacement influence coefficient matrix, and $\mathbf{G}^{MM}$ is the surface traction influence coefficient matrix; $\mathbf{u}^M$ is the nodal displacement column vector, and $\mathbf{p}^M$ is the nodal surface traction column vector of all nodes; the column vector $\mathbf{a}^M$ is only related to the responses of the first $M-1$ time steps, as follows.

$$\mathbf{a}^M = \sum_{m=0}^{M-1} (-\overline{\mathbf{H}}^{Mm}\mathbf{u}^m + \mathbf{G}^{Mm}\mathbf{p}^m) \tag{23}$$

5.2. Solution of the Algebraic Equation System

There is a possibility of unknown quantities in both $\mathbf{u}^M$ and $\mathbf{p}^M$. Therefore, Equation (22) needs to be rearranged into the standard form, where the unknown and known quantities are separated into the left and right sides of the equation system, respectively. The solving processes are as follows.

1. Standard form of algebraic equation system

Exchange the known quantities in $\mathbf{u}^M$ and the unknown quantities in $\mathbf{p}^M$, while exchanging the corresponding columns of $\mathbf{H}^{MM}$ and $\mathbf{G}^{MM}$, and changing their signs. Then, $\mathbf{u}^M$ and $\mathbf{p}^M$ are transformed into a column vector $\mathbf{x}^M$ (containing all boundary unknowns) and a column vector $\mathbf{y}_0^M$ (containing all knowns), respectively; meanwhile $\mathbf{H}^{MM}$ and $\mathbf{G}^{MM}$ are transformed into $\mathbf{A}_1^{MM}$ and $\mathbf{A}_2^{MM}$, respectively. Let $\mathbf{y}^M = \mathbf{A}_2^{MM}\mathbf{y}_0^M + \mathbf{a}^M$, then the standard form of Equation (22) is obtained as Equation (24).

$$\mathbf{A}_1^{MM}\mathbf{x}^M = \mathbf{y}^M \tag{24}$$

2. The unknown displacements and surface tractions of boundary nodes

The unknown vector $\mathbf{x}^M$ can be solved by Equation (25), then combined with boundary conditions, the displacements and surface tractions of all boundary nodes can be obtained.

$$\mathbf{x}^M = (\mathbf{A}_1^{MM})^{-1}\mathbf{y}^M \tag{25}$$

3. The displacements and stresses of interior points

After solving the displacements and surface tractions of all boundary nodes, the displacements and stresses of interior points can be obtained by the interior point boundary integral equation (see [30]). Since the interior points are unable to coincide with the boundary nodes, the interior point boundary integral equation does not contain spatial singularity.

6. Verification

Three typical elastodynamic problems are selected for verification, namely a fixed–fixed beam under a uniformly applied sudden load, an infinite domain with a single cavity subjected to blasting load on its boundary, and a double tunnel beneath valley topography subjected to metro vibration load. These problems involve typical scenarios of finite, infinite and semi-infinite domains, as well as both simple and complex geometric boundary configurations. Since the proposed treatment for logarithmic singularities is applied only to a small number of singular elements where the source point coincides with element nodes, while the majority of non-singular elements remain identical to those in the conventional TD-BEM, the additional computational cost is negligible. Therefore, no separate efficiency study is required. The robustness and correctness of the proposed method are verified by comparing the results with reference solutions obtained from the method of characteristics [31] and FEM. For cases where analytical solutions are available, the method of characteristics is used, while FEM results are used as reference when analytical solutions are not available.

6.1. Robustness Analysis

To verify the numerical robustness of the proposed method, an infinite domain model with a single cavity is established, and blasting loads are applied on the cavity boundary, as illustrated in Figure 5. The radius of the cavity r_0 = 1 m, and the blasting load $p(t) = 1.435p_0 \times (\mathrm{e}^{-1279t} - \mathrm{e}^{-12792t})$, with p_0 = 50 MPa, as shown in Figure 6. Poisson's ratio, Young's modulus and density of the material are ν = 0.25, $E = 4.0 \times 10^{10}$ N/m^2 and $\rho = 2.8 \times 10^3$ kg/m^3. The P-wave velocity can be correspondently determined as v_d = 4140 m/s. The cavity boundary is discretized by 20, 28, 40 linear boundary elements, respectively. The spatial mesh discretization of the cavity boundary is illustrated in Figure 7, where boundary elements are sequentially discretized in a clockwise direction. The time step is set to 5×10^{-5} s, 3.5×10^{-5} s, 2.5×10^{-5} s. The discretization coefficient β ranges from 0.33 to 1.32 [10].

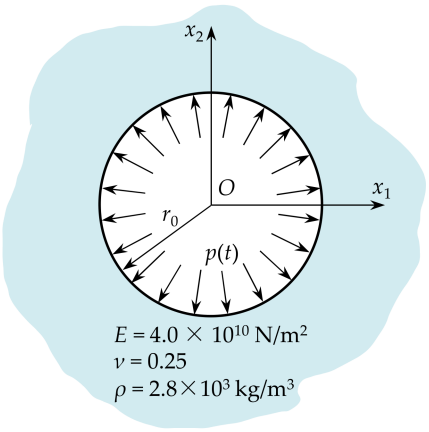


Figure 5. Diagram of infinite domain with a cavity subjected to a uniform blasting load.

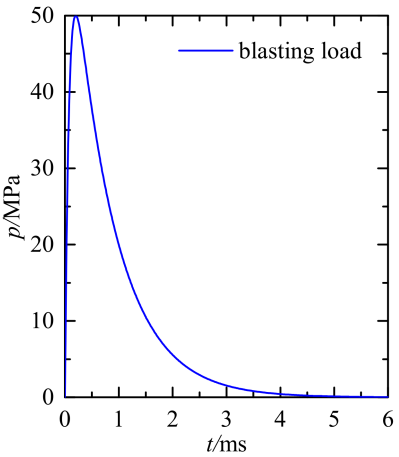


Figure 6. Time history curve of blasting load.

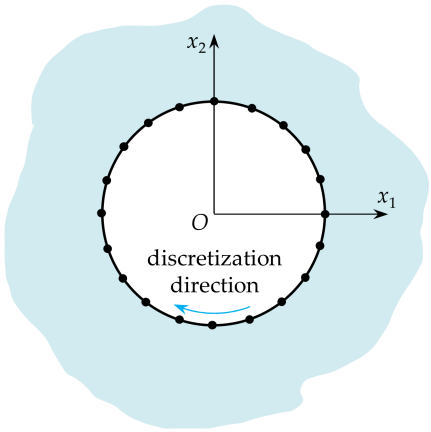


Figure 7. Schematic diagram of spatial mesh discretization.

The peak radial displacement at the circular contour of r = 2 m is extracted. By sequentially reducing the time step and spatial mesh size at a scaling factor of approximately 0.7, the variation characteristics of dynamic responses are analyzed. The relative errors are computed by comparison with the analytical solution from the method of characteristics. The peak radial displacement and relative error on the circle with radius r = 2 m are illustrated in Table 1.

Table 1. Peak radial displacement and relative error on the circle with radius r = 2 m.

Spatial and Temporal Discretization		Total Number of Spatial Meshes		
		20	**28**	**40**
Time step (s)	5×10^{-5} s	0.79500 (2.15%)	0.80606 (0.785%)	0.81062 (0.224%)
	3.5×10^{-5} s	0.79705 (1.89%)	0.80761 (0.594%)	0.81237 (0.009%)
	2.5×10^{-5} s	0.79724 (1.87%)	0.80799 (0.547%)	0.81237 (0.009%)
Method of Characteristics		0.81244		

Note that the values in parentheses denote the relative errors of TD-BEM numerical solutions against analytical results from the method of characteristics.

It can be seen from Table 1 that the peak radial displacement at r = 2 m gradually converges to the analytical solution from the method of characteristics, and the corresponding relative error continuously declines with the refinement of spatial meshes and the reduction in time steps. Notably, the numerical accuracy presents a more rapid improvement with the decreasing mesh size, whereas the convergence rate induced by temporal time-step adjustment is relatively mild and slow. As the total mesh number increases from 20 to 40 and the time step decreases from 5×10^{-5} s to 2.5×10^{-5} s, the maximum relative error drops from 2.15% to merely 0.009%. No numerical oscillation or divergence occurs during parameter variation, and the numerical results maintain stable and monotonic convergence. The above results demonstrate that the proposed TD-BEM algorithm possesses favorable robustness against spatial and temporal discretization variations.

When the spatial mesh quantity is 20 and the time step is set as 5×10^{-5} s, namely β = 0.66, the calculation relative error is already controlled about 2%, achieving satisfactory high computational precision. Accordingly, the time-history curves of radial displacement and stress on the circular contour of r = 2 m under this discrete scheme are illustrated in Figure 8, to further verify the full-time-domain calculation accuracy of the proposed algorithm. The curve labeled "Characteristics" represents the analytical solution obtained by the method of characteristics [31].

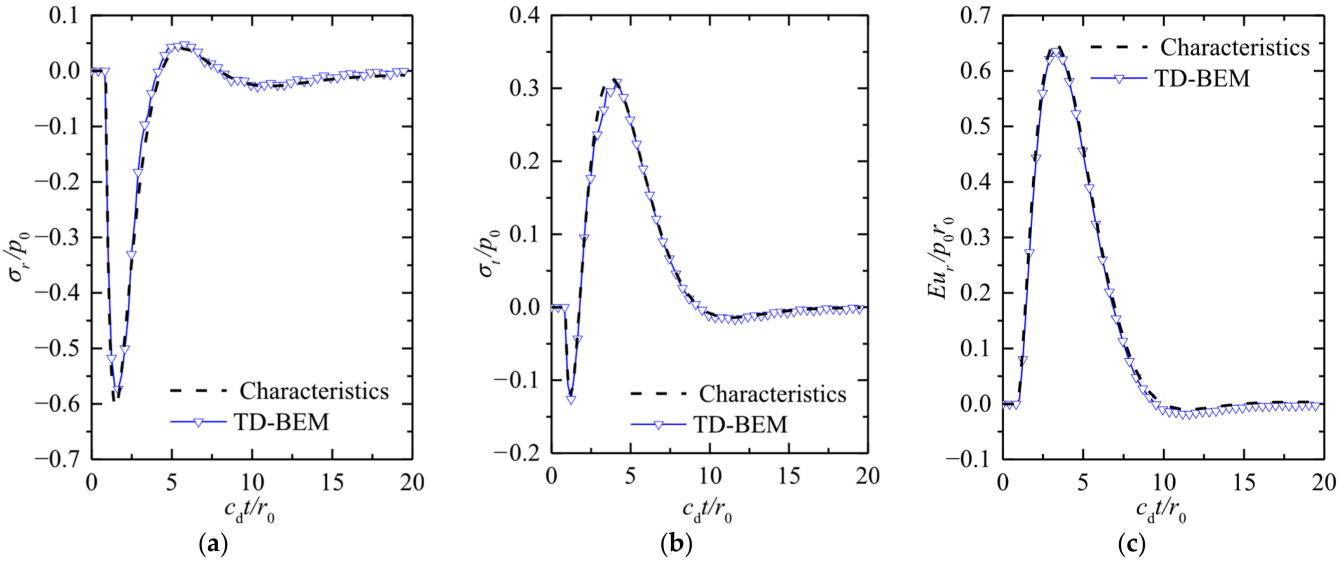


Figure 8. Stress and displacement curves of a circle with r = 2 m (each triangular marker represents two discrete time steps): (**a**) radial stress curves; (**b**) tangential stress curves; (**c**) displacement curves.

6.2. Accuracy Analysis

6.2.1. Fixed–Fixed Beam Subjected to a Uniform Sudden Load

The diagram of fixed–fixed beam is as Figure 9, where a = 1 m, and the sudden load $p(t)$ = 200 MPa for $t \geq 0$, as shown in Figure 10. Poisson's ratio, Young's modulus and density of the material are $\nu = 0.3$, $E = 2.1 \times 10^{11}$ N/m^2 and $\rho = 7.9 \times 10^3$ kg/m^3. The P-wave velocity can be correspondingly determined as $v_d = 5982$ m/s. Based on the symmetry, the semi-structure is adopted to reduce the computational complexity, and the meshes and corresponding boundary constraints are shown in Figure 11. A total of 30 linear boundary elements with an individual of 0.2 m are adopted to discretize the boundary domain, and the time step is set to 2.5×10^{-5} s. The discretization coefficient $\beta = 0.75$ [10]. The displacement results of the middle span of point A are shown in Figure 12, where u_0 represents the static solution of point A [32].

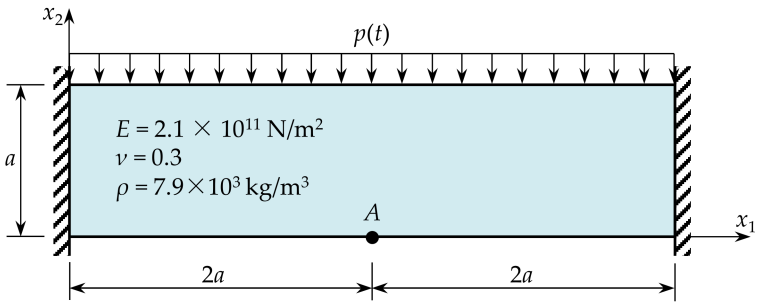


Figure 9. Diagram of fixed–fixed beam suffered from sudden load.

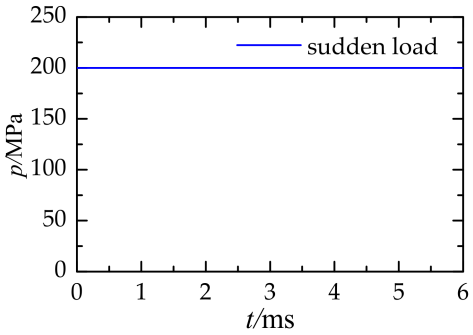


Figure 10. Time history curve of sudden load.

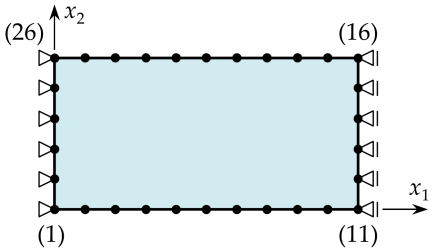


Figure 11. Meshes and constrained for semi-structure.

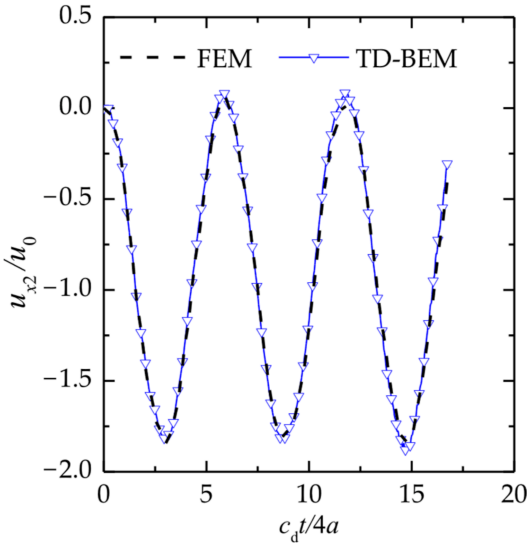


Figure 12. Displacement curves for mid span point A (each triangular marker represents two discrete time steps).

6.2.2. Double Tunnel Beneath Valley Topography Subjected to Metro Vibration Load

The diagram of the double tunnel beneath valley topography is shown in Figure 13, where the centers of the two tunnels are $O_1(-8\text{ m}, 0)$ and $O_2(8\text{ m}, 0)$, and the radius $r_0 = 3$ m, the central angle $\theta = \pi/3$. The coordinates of key points on the ground are presented as follows (unit: m): $B_1(100, 16)$, $B_2(52, 16)$, $B_3(10, 16)$, $B_4(9, 18)$, $B_5(7, 18)$, $B_6(1, 12)$, $B_7(-4, 12)$, $B_8(-7, 18)$, $B_9(-9, 18)$, $B_{10}(-10, 16)$, $B_{11}(-52, 16)$, $B_{12}(-100, 16)$. The time history curve of vibration load $p(t)$ caused by metro operation is shown in Figure 14. Poisson's ratio, Young's modulus and mass density of the material are $\nu = 0.25$, $E = 2.2 \times 10^7$ N/m^2 and $\rho = 1.8 \times 10^3$ kg/m^3. The P-wave velocity can be correspondently determined as $v_d = 121$ m/s. The meshes are shown in Figure 15. The element size along B_1B_2 and $B_{11}B_{12}$ is 3 m, while that along B_2B_3 and $B_{10}B_{11}$ is 2 m. The mesh size along the valley boundary B_3B_{10} ranges from 1 m to 1.5 m. Each inner boundary of the tunnel is discretized into 24 elements, with an approximate element length of 0.8 m. The radiation conditions of the semi-infinite far domain are simulated by two adaptive semi-infinite boundary elements (ASIBE) [33]. The time step is set to 1.25×10^{-2} s. The discretization coefficient $\beta = 0.76$ [10]. The displacement of point $O_3(0, 16)$ on the ground is shown in Figure 16.

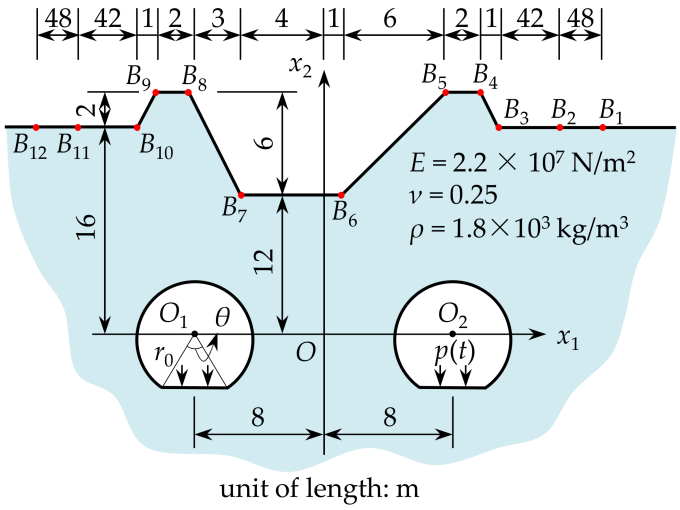


Figure 13. Diagram of semi-infinite domain with two cylindrical cavities subjected to metro vibration load.

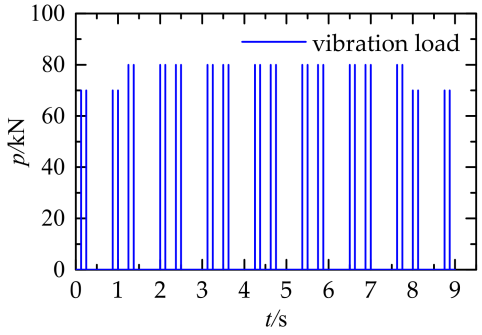


Figure 14. Vibration load caused by metro operation.

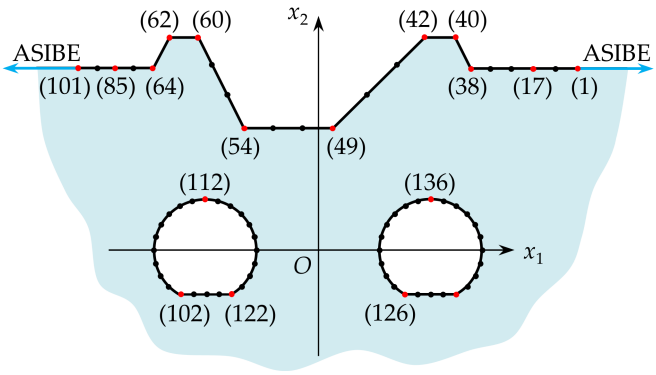


Figure 15. Mesh diagram for double tunnel beneath valley topography.

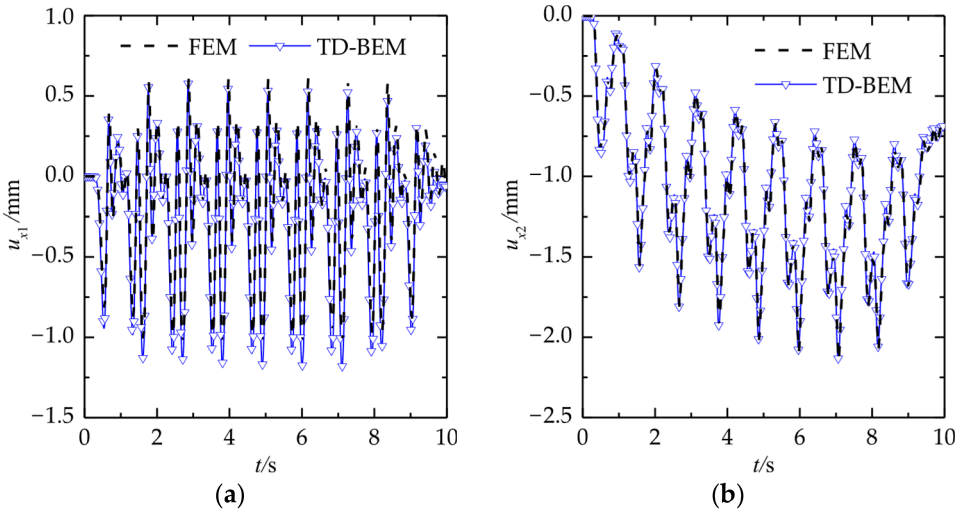


Figure 16. Displacement curves of point B_8 (each triangular marker represents four discrete time steps): (**a**) horizontal displacement curves; (**b**) vertical displacement curves.

6.2.3. Discussion

In this paper, three types of typical dynamic engineering problems, covering finite domain, infinite domain, and semi-infinite domain, are selected as verification examples in a targeted manner. These include a fixed–fixed beam under a uniform sudden load, an infinite domain with a cavity subjected to boundary blasting load, and a double tunnel beneath valley topography subjected to metro vibration load. These three examples correspond to the typical scenarios in structural dynamics, blasting dynamics, and environmental vibration engineering of urban rail transit, which can comprehensively verify the applicability and correctness of the established analytical integration formulas for logarithmic spatial singularities under different spatial domain types.

The numerical calculation results show that the results obtained by the proposed method in the three examples are in good agreement with the reference solutions: in the fixed–fixed beam example of the finite domain, the displacement time-history curve of the mid-span node is highly consistent with the reference solution, which verifies the accuracy of the formulas in handling logarithmic spatial singularities in the calculation of structural dynamic responses in finite domains. In the cavity blasting example of the infinite domain, the calculated results of radial stress, tangential stress and displacement on the circle 2 m away from the cavity center (r = 2 m) are consistent with the reference solutions, reflecting that the proposed formulas preserve the intrinsic properties of TD-BEM, which inherently satisfy far-field radiation conditions for infinite domains. Meanwhile, they guarantee high-precision singular integral calculations for elastodynamic problems with infinite domains. In the example of the double tunnel beneath valley topography subjected to metro vibration load, the displacement time-history results of the specified ground measuring point are in good agreement with the reference solution, which proves that the proposed formulas can still effectively solve the problem of logarithmic spatial singularities in engineering problems of semi-infinite domains combined with complex multi-cavity boundaries, and the calculation results are stable.

The consistent verification results of the above three examples with different spatial domain types fully demonstrate the mathematical correctness and engineering applicability of the analytical integration formulas for logarithmic spatial singularities established in this paper. These formulas can effectively handle the logarithmic spatial singular integrals in TD-BEM and provide a reliable singular integral treatment method for the TD-BEM numerical calculation of elastodynamic problems involving different spatial domain types.

7. Conclusions

Aiming at the challenge of handling logarithmic spatial singular integrals in TD-BEM for solving elastodynamic problems, this paper derives and establishes a set of analytical integration formulas based on the properties of the Heaviside function, which enables the direct spatiotemporal analytical solution of such singular integrals. The formulas are verified by three typical elastodynamic examples covering finite, infinite and semi-infinite domains. The main conclusions are as follows:

1. The derivation process of the formulas is mathematically rigorous, which provides a direct analytical solution for logarithmic spatial singular integrals in TD-BEM;
2. The formulas fundamentally avoid the accuracy-influencing factors of numerical integration methods in dealing with singular problems, further improve the theoretical system of singular integral treatment in TD-BEM, and provide a reliable approach for solving singular integrals for its engineering application;
3. The robustness, correctness and engineering applicability of the proposed analytical integration formulas are fully verified, with the calculated results in good agreement with the reference solutions. The formulas can effectively handle logarithmic spatial singular integrals in TD-BEM for different spatial domain types, and are applicable to the calculation of elastodynamic problems in various scenarios such as structural dynamics, blasting dynamics and urban rail transit environmental vibration.

The proposed analytical integration formulas for logarithmic spatial singularities provide important theoretical support for the numerical application of TD-BEM in elastodynamic problems. In the present study, the formulation is developed for 2D linear elastodynamic problems using linear elements. The approach can be extended to higher-order isoparametric elements and 3D elastodynamic problems through the derivation of the corresponding analytical expressions for singular integrals. This will be a main direction of our future work.

https://doi.org/10.3390/mca31030068

Author Contributions: Conceptualization, H.L.; methodology, F.Z.; software, X.L.; validation, X.L.; formal analysis, X.L.; investigation, W.L.; resources, W.L.; data curation, F.Z.; writing—original draft preparation, F.Z.; writing—review and editing, H.L.; supervision, J.L.; project administration, J.L.; funding acquisition, W.L. and H.L. All authors have read and agreed to the published version of the manuscript.

Funding: This research was funded by National Natural Science Foundation of China, grant number 12471497, and Guangzhou Metro Design and Research Institute Co., Ltd. of China, grant number KY-2022-014 and The APC was funded by 12471497.

Data Availability Statement: The data used to support the findings of this study are included within the article. All numerical results and validation data are presented in the figures of the paper. Further inquiries can be directed to the corresponding author.

Conflicts of Interest: The authors declare that they have no known competing financial interests or personal relationships that could have appeared to influence the work reported in this paper.

Abbreviations

The following abbreviations are used in this manuscript:

TD-BEM	Time Domain Boundary Element Method
FEM	Finite Element Method
FDM	Finite Difference Method
BEM	Boundary Element Method
ASIBE	Adaptive Semi-Infinite Boundary Element

References

1. Dominguez, J. *Boundary Elements in Dynamics*; Computational Mechanics Publications; Elsevier Applied Science: Southampton, UK; London, UK, 1993.
2. Manolis, G.D. A comparative study on three boundary element method approaches to problems in elastodynamics. *Int. J. Numer. Methods Eng.* **1983**, *19*, 73–91. [CrossRef]
3. Guiggiani, M.; Krishnasamy, G.; Rudolphi, T.J.; Rizzo, F.J. A general algorithm for the numerical solution of hypersingular boundary integral equations. *J. Appl. Mech.* **1992**, *59*, 604–614. [CrossRef]
4. Guiggiani, M.; Gigante, A. A general algorithm for multidimensional Cauchy principal value integrals in the boundary element method. *J. Appl. Mech.* **1990**, *57*, 906–915. [CrossRef]
5. Niu, Z.R.; Zhou, H.L. The natural boundary integral equation in potential problems and regularization of the hypersingular integral. *Comput. Struct.* **2004**, *82*, 315–323. [CrossRef]
6. Xie, G.Z.; Zhou, F.L.; Zhong, Y.D. Bi–directional sinh transformations based on the generalized Duffy space for nearly singular integrals. *J. Comput. Appl. Math.* **2020**, *380*, 112981. [CrossRef]
7. Xie, G.Z.; Li, K.; Zhong, Y.D.; Zhou, F.L. A systematic derived sinh based method for singular and nearly singular boundary integrals. *Eng. Anal. Bound. Elem.* **2021**, *123*, 147–153. [CrossRef]
8. Giannopoulos, G.I.; Anifantis, N.K. A BEM analysis for thermomechanical closure of interfacial cracks incorporating friction and thermal resistance. *Comput. Methods Appl. Mech. Eng.* **2007**, *196*, 1018–1029. [CrossRef]
9. Mansur, W.J.; Brebbia, C.A. Formulation of the boundary element method for transient problems governed by the scalar wave equation. *Appl. Math. Model.* **1982**, *6*, 307–311. [CrossRef]
10. Mansur, W.J.; Brebbia, C.A. Numerical implementation of the boundary element method for two dimensional transient scalar wave propagation problems. *Appl. Math. Model.* **1982**, *6*, 299–306. [CrossRef]
11. Mansur, W.J. A Time–Stepping Technique to Solve Wave Propagation Problems Using the Boundary Element Method. Ph.D. Thesis, University of Southampton, Southampton, UK, 1983.
12. Mansur, W.J.; Brebbia, C.A. Transient elastodynamics using a time stepping technique. In *Boundary Elements*; Springer: Berlin/Heidelberg, Germany, 1983.
13. Mansur, W.J.; Brebbia, C.A. Further developments on the solution of the transient scalar wave equation. In *Time-Dependent and Vibration Problems*; Brebbia, C.A., Ed.; Springer: Berlin/Heidelberg, Germany, 1985; Volume 2.
14. Mansur, W.J.; Brebbia, C.A. Transient elastodynamics. In *Time-Dependent and Vibration Problems*; Brebbia, C.A., Ed.; Springer: Berlin/Heidelberg, Germany, 1985; Volume 2.

15. Lei, W.D.; Ji, D.F.; Li, H.J.; Li, Q.X. On an analytical method to solve singular integrals both in space and time for 2-D elastodynamics by TD-BEM. *Appl. Math. Model.* **2015**, *39*, 6307–6318. [CrossRef]
16. Lei, W.D.; Li, H.J.; Qin, X.F. Dynamics-based analytical solutions to singular integrals for elastodynamics by time domain boundary element method. *Appl. Math. Model.* **2018**, *56*, 612–625. [CrossRef]
17. Xie, G.Z.; Zhong, Y.D.; Zhou, F.L. Singularity cancellation method for time-domain boundary element formulation of elastodynamics: A direct approach. *Appl. Math. Model.* **2020**, *80*, 647–667. [CrossRef]
18. Zhong, Y.D.; Hou, J.J.; Xie, G.Z. A method for dealing with singular integrals in the elastodynamics boundary element method. *Chin. J. Comput. Mech.* **2023**, *40*, 66–72. [CrossRef]
19. Telles, J.C.F. *The Boundary Element Method Applied to Inelastic Problems*; Springer: Berlin/Heidelberg, Germany; New York, NY, USA; Tokyo, Japan, 1983.
20. Telles, J.C.F.; Brebbia, C.A. On the application of the boundary element method to plasticity. *Appl. Math. Model.* **1979**, *3*, 466–470. [CrossRef]
21. Banerjee, P.K.; Henry, D.P.; Raveendra, S.T. Advanced inelastic analysis of solids by the boundary element method. *Int. J. Mech. Sci.* **1989**, *31*, 309–322. [CrossRef]
22. Deng, Q.; Li, C.G.; Wang, S.L. Nonlinear complementarity approach for elastoplastic BEM without internal cell. *Eng. Mech.* **2012**, *29*, 49–55. [CrossRef]
23. Li, H.J.; Lei, W.D.; Zhou, H. Analytical treatment on singularities for 2-d elastoplastic dynamics by time domain boundary element method using Hadamard principle integral. *Eng. Anal. Bound. Elem.* **2021**, *129*, 93–104. [CrossRef]
24. Li, H.J.; Lei, W.D.; Chen, R. A study on boundary integral equations for dynamic elastoplastic analysis for the plane problem by TD-BEM. *Acta Mech. Sin.* **2021**, *37*, 662–678. [CrossRef]
25. Johnston, P.R.; Elliott, D. A generalisation of Telles' method for evaluating weakly singular boundary element integrals. *J. Comput. Appl. Math.* **2001**, *131*, 223–241. [CrossRef]
26. Telles, J.C.F. A self-adaptive coordinate transformation for efficient numerical evaluation of general boundary element integrals. *Int. J. Numer. Meth. Eng.* **1987**, *24*, 959–973. [CrossRef]
27. Smith, R.N.L. Direct Gauss quadrature formulae for logarithmic singularities on isoparametric elements. *Eng. Anal. Bound. Elem.* **2000**, *24*, 161–167. [CrossRef]
28. Yu, G.; Mansur, W.J.; Carrer, J.A.M.; Lie, S.T. A more stable scheme for BEM/FEM coupling applied to two-dimensional elastodynamics. *Comput. Struct.* **2001**, *79*, 811–823. [CrossRef]
29. Carrer, J.A.M.; Mansur, W.J. Time discontinuous linear traction approximation in time-domain BEM: 2-D elastodynamics. *Int. J. Numer. Meth. Eng.* **2000**, *49*, 833–848. [CrossRef]
30. Carrer, J.A.M.; Mansur, W.J. Stress and velocity in 2D transient elastodynamic analysis by the boundary element method. *Eng. Anal. Bound. Elem.* **1999**, *23*, 233–245. [CrossRef]
31. Chou, P.C.; Koenig, H.A. A unified approach to cylindrical and spherical elastic waves by method of characteristics. *J. Appl. Mech.* **1966**, *33*, 159–167. [CrossRef]
32. Carrer, J.A.M.; Fleischfresser, S.A.; Garcia, L.F.T. Dynamic analysis of Timoshenko beams by the boundary element method. *Eng. Anal. Bound. Elem.* **2013**, *37*, 1602–1616. [CrossRef]
33. Li, H.J.; Yang, J.Q.; Liu, J.C. Environmental vibration simulation of metro operation based on multi-boundary problem time domain boundary element method. *Eng. Anal. Bound. Elem.* **2025**, *176*, 106249. [CrossRef]

Disclaimer/Publisher's Note: The statements, opinions and data contained in all publications are solely those of the individual author(s) and contributor(s) and not of MDPI and/or the editor(s). MDPI and/or the editor(s) disclaim responsibility for any injury to people or property resulting from any ideas, methods, instructions or products referred to in the content.